Porous Defective Bi/Bi₃NbO₇ Nanosheets for Efficient Photocatalytic NO Removal under Visible Light

Ting Gao [1,†] [iD]**, Jingqi Lin** [1,†]**, Ke Zhang** [1]**, Mohsen Padervand** [2,*]**, Yifan Zhang** [3]**, Wei Zhang** [1]**, Menglin Shi** [4]
and Chuanyi Wang [1,*] [iD]

1 School of Environmental Science and Engineering, Shaanxi University of Science and Technology, Xi'an 710021, China
2 Department of Chemistry, Faculty of Science, University of Maragheh, Maragheh P.O. Box 55181-83111, Iran
3 Xi'an Institute for Innovative Earth Environment Research, Xi'an 710061, China
4 Missile Engineering College, Rocket Force University of Engineering, Xi'an 710025, China
* Correspondence: padervand@maragheh.ac.ir (M.P.); wangchuanyi@sust.edu.cn (C.W.)
† These authors contributed equally to this work.

Abstract: Since conventional techniques are ineffective for NO removal at low concentrations, photocatalysis has become attractive in this regard, recently. However, in practice, photocatalytic NO removal has drawbacks such as limited light absorption and the proclivity of producing toxic by-products. To address these issues, novel defective Bi/Bi₃NbO₇ structures with good porosity were fabricated by a solvothermal method and used for enhanced photocatalytic NO removal under visible light irradiation. The morphological and structural properties of the prepared materials were comprehensively analyzed. The optimal photocatalytic activity of pore-defective Bi/Bi₃NbO₇ for NO removal was 60.3%, when the molar ratios of urea and Bi(NO)₃•5H₂O to pristine Bi₃NbO₇ were 1:25 and 1:2, respectively, under the following operational conditions: NO concentration of 700 ppb, catalyst dosage of 50 mg and irradiation time of 14 min. The induced defects and the surface plasmon resonance (SPR) effect of Bi nanodots made remarkable contributions to improving the photocatalytic NO removal as well as inhibiting the toxic byproduct NO₂. The photocatalytic NO removal pathway over the prepared photocatalysts was further mechanistically clarified taking advantage of EPR results and scavenging experiments. Considering the increased NO generation in the atmosphere, this work may provide novel insights for designing effective porous photocatalysts to treat gaseous toxic pollutants.

Keywords: photocatalysis; Bi₃NbO₇; surface plasmon resonance; NO removal; defects

1. Introduction

As a kind of typical air pollution, nitrogen oxides (NOx) are generated from the combustion of fossil energy. NOx mainly consist of NO and NO₂, which can cause acid rain, photochemical smog and other environmental issues [1]. Hence, it is highly important to protect the atmosphere around the world from increasingly emissions of NO through developing effective technologies to relieve NOx pollution [2]. Up to now, many studies have revealed that conventional NO removal technologies, e.g., biofiltration, physical adsorption and thermal catalysis, perform well at high NOx concentration levels but are not much efficient for the treatment of low concentrations in practical applications [3].

Recently, researchers have found that photocatalysis could be sufficiently promising for removing NOx at ppb levels and thus appears as a sustainable, energy-effective and ecologically friendly method to purify the environment [3–6]. TiO₂, the pioneer photocatalyst, has been widely used in NO pollution treatment. However, given its large band gap (~3.0 eV for rutile and ~3.2 eV for anatase), TiO₂ can only absorb ultraviolet light photons during the catalytic reactions, which makes its practical application restricted. In order to overcome this obstacle, many efforts have been made to develop visible light-driven

photocatalysts, including doping impurities [7,8], sensitization [9], and heterojunctions construction [10]. However, these modification techniques suffer from issues including thermal instability, rapid electron-hole recombination, high cost of metal sources, and so on [11,12]. To address these issues, developing novel semiconducting materials is always demanded.

Bi_3NbO_7 (E_g~2.9 eV), an n-type semiconductor, has attracted a lot of interest because of its superior interaction with visible light photons and good photocatalytic performance [13,14]. The valence band of Bi_3NbO_7 is formed by the hybridization of Bi 6s and O 2p orbitals, resulting in high oxidation activity and charge separation efficiency. Interestingly, Bi_3NbO_7 possesses a layered structure which justifies its high specific surface area for heterogeneous photocatalytic reactions. However, the traditional methods of Bi_3NbO_7 preparation always are accompanies by some drawbacks such as the tough two-step synthesis, the use of toxic solvents such as hydrofluoric acid during the preparation, and poor chemical stability of the structure under irradiation [15]. Therefore, it is urgent to develop well-modified niobate photocatalysts that are easy to prepare, non-hazardous, and highly stable.

Noble metal-loaded semiconductors can improve the separation of photogenerated charge carriers and the visible light harvesting properties by surface plasmon resonance (SPR) effects, but their high costs limit the technology's development toward practical applications [16,17]. Interestingly, the cheaper metallic bismuth (Bi), aluminum (Al) and titanium nitride (TiN) have been shown to act well as effective alternatives to noble metals due to their intense SPR effect [18–20]. Moreover, porous defects insertion into the bulk structure is indicated to be a reliable strategy to ameliorate the photocatalytic performance of various kinds of semiconductors [21,22]. The aforementioned defects can increase the specific surface area, improve the substrates' adsorption on the surface and act as remarkable catalytic active sites to promote the subsequent oxidation of pollutants [23]. Based on previous works, urea, a low-cost, environmentally friendly and easily available porogenic agent, can serve to control the pore size of solid materials [24,25]. For instance, Wang et al. successfully fabricated porous Bi_3NbO_7 nanosheets by adjusting the urea content towards the photodegradation of dye compounds under visible light [13]. Overall, metallic Bi and porous defects show incredible synergetic effects to ameliorate the photocatalytic performance of pristine semiconductors under visible light irradiation.

In this work, 2D pore-defective Bi/Bi_3NbO_7 nanomaterials were successfully prepared from niobium oxalate, as the raw niobium source, and urea in the presence of a Bi source via solvolysis. With the change of the urea content, the morphology of Bi_3NbO_7 gradually showed the growth of porous defects in the structure, which occurred along with the enhancement of visible light photoactivity. Meanwhile, the pore-defective Bi/Bi_3NbO_7 exhibited a much more efficient photocatalytic performance for NO conversion when an appropriate amount of Bi nanoparticles was introduced. The synergistic interaction of metallic Bi and porous defects was shown to serendipitously affect the electronic properties, leading to the better light-harvesting capacity and charge carriers separation. Interestingly, NO_2 formation was significantly inhibited compared to that of observed for the other photocatalysts, which is of great importance to minimize the harmful effects of intermediates. The mechanism of enhanced photoactivity compared to that of pore-defective Bi/Bi_3NbO_7 nanosheets is also discussed based on the EPR analysis and trapping tests.

2. Experimental Methods

2.1. Chemicals

Bismuth nitrate pentahydrate ($Bi(NO)_3 \bullet 5H_2O$), urea ($CO(NH_2)_2$), niobium oxalate ($C_{10}H_5NbO_{20}$), potassium hydroxide (KOH), potassium dichromate ($K_2Cr_2O_7$) and potassium iodide (KI) were purchased from Shanghai Macklin Biochemical Co., Ltd. Acetic acid was obtained from Sinopharm Chemical Reagent Co., Ltd. Ethanol was obtained from Tianjin Fuyu Fine chemical Co., Ltd. Ethylene glycol, tert-butyl acrylate (TBA) and P-benzoquinone (PBQ) were obtained from Shanghai Rhawn Chemical Technology Co., Ltd.

Methanol and benzyl alcohol were obtained from Aladdin Reagent Co., Ltd. All chemicals in this work were of analytical grade and used without further purification.

2.2. Photocatalyst Preparation

2.2.1. Synthesis of Bi_3NbO_7

We dissolved 3 mmol of $Bi(NO)_3 \bullet 5H_2O$ (1.46 g) in 10 mL of acetic acid, obtaining solution A. To prepare solution B, 1 mmol of niobium oxalate (0.54 g) was added to 20 mL of methanol. Under vigorously swirling, solution A was slowly drizzled into solution B. Then, urea (0, 0.8, 1.6 and 3.2 g) was added to the mixed solution, obtaining the solutions called BNO, 1-BNO, 2-BNO and 3- BNO, respectively. The pH of all mixtures was adjusted to 13 with a KOH solution. Each suspension was then transferred to a 100 mL polytetrafluoroethylene reaction tank and kept at 180 °C for 24 h. After cooling to room temperature, the samples were washed repeatedly with deionized water and ethanol, and then dried at 60 °C for 6 h.

2.2.2. Synthesis of $Bi@Bi_3NbO_7$

We dispersed 0.4 g of the as-obtained Bi_3NbO_7 powder in 60 mL of ethylene glycol to form a homogeneous suspension. A certain amount of $Bi(NO)_3 \bullet 5H_2O$ was then added to the suspension, which was stirred for 30 min. The suspension was transferred to a 100 mL polytetrafluoroethylene reaction tank and kept at 180 °C for 8 h. After the completion of the reaction, the suspension was repeatedly washed and centrifuged (8 times) to obtain a precipitate which was finally dried at 60 °C for 6 h, yielding the pore-defective $Bi@Bi_3NbO_7$ nanosheets. Three samples with different Bi nanodot loadings, labeled as 1% Bi-2-BNO, 2% Bi-2-BNO and 4% Bi-2-BNO, were prepared from 0.04, 0.1 and 0.2 g of $Bi(NO)_3 \bullet 5H_2O$, respectively.

2.3. Characterization

A Bruker D8 Advance X-ray diffractometer (λ = 0.15406 nm) at 127 40 kV and 40 mA over a 2θ range from 10 to 80° (Bruker, Karlsruhe, Baden-Württemberg, Germany) was utilized to provide XRD patterns. A FEI Talos F200X (Thermo Fisher Scientific, Hillsboro, OR, USA) microscope was used to perform high-resolution transmission electron microscopy (HRTEM) and morphological analyses. The sample powder was dispersed in ethanol before being placed as a very diluted suspension onto a copper grid. Using 3–5 KV accelerating voltage, a scanning electron microscope (ZEISS Sigma 300, Carl Zeiss, Jena, Thuringia, Germany) was used to examine the samples' microstructure and average size. Using $BaSO_4$ as the background, a Shimadzu UV-2550 spectrophotometer (Shimadzu, Kyoto, Japan) was used to examine the diffuse reflectance spectra (DRS) in the UV–Vis range. Under Al Ka radiation as the excitation source, X-ray photoelectron spectroscopy (XPS) data were supplied to a VG Multilabel 2000 ((Thermo Fisher Scientific, Waltham, MA, USA) photoelectron spectrometer. Using the contaminant carbon's (C 1s 284.8 eV) binding energy as the reference, all binding energies were calibrated. A Micromeritics ASAP 2460 (Micromeritics, Norcross, GA, USA) gas adsorption–desorption device, the Brunauer–Emmett–Teller (BET) specific surface areas were determined through the nitrogen adsorption–desorption isotherms. Using DMPO as the trapping agent, the Bruker E500 (Bruker, Karlsruhe, Baden-Württemberg, Germany) instrument was used to conduct electron paramagnetic resonance (EPR) investigations, while the suspensions were prepared in a 40 mM DMPO solution using water as a solvent for DMPO$-\bullet$OH and methanol for DMPO$-\bullet O_2^-$. A 5 mol$\cdot$L^{-1} aqueous solution of Na_2SO_4, as the reference electrolyte, was used in the photoelectrochemical (PEC) measurements over a CHI660E electrochemical workstation (Chenhua Instruments, Inc., Shanghai, China).

2.4. Photocatalytic NO Removal

The photocatalytic setup consisted of a gas supply system, an airflow meter, the main reactor, a light source and the NOx analyzer. The gas supply system provided NO gas with a concentration of 100 ppm and clean dry air. The gases from the gas supply system

were well mixed in the airflow meter at a gas flow rate of 300 mL·min^{-1}, adjusting the NO concentration level at 700 ppb. The photocatalytic reactor was made from a cylindrical quartz reactor with the volume of 150 mL. The light source was a xenon lamp with a 420 nm cut-off filter, which was operated at 300 W and 20 mA to keep the light density and intensity consistent throughout the study. The NOx analyzer was able to track the concentration of both NO and NO$_2$ continuously. First of all, 50 mg of the powder sample was uniformly dispersed in a Petri dish with 6.0 cm of diameter (Figure 1). A drying device was added prior to NOx analysis to remove water vapor from the inlet gas. All devices in the photocatalytic efficiency evaluating system were connected to polytetrafluoroethylene hoses, and each interface was sealed by sealing tape to ensure that there were no leaks in the system. The obtained coated dish was placed in the center of the photocatalytic reactor. The above-described setup for photocatalytic NO removal is schematically displayed in Figure 2. The photocatalytic efficiency, η, was calculated using the following equation:

$$\eta = \frac{C}{C_0} \times 100\% \tag{1}$$

$$\eta = \frac{C}{C_0} \times 100\% \tag{2}$$

where C and C$_0$ correspond to the concentrations of NO before and after the photocatalytic test. The concentration of the toxic by-product NO$_2$ was calculated according to the following equation:

$$C_{NO_2}(ppb) = C_{NO_x} - C_{NO} \tag{3}$$

where C$_{NO_x}$ and C$_{NO}$ stand for the concentrations of NOx and NO, respectively.
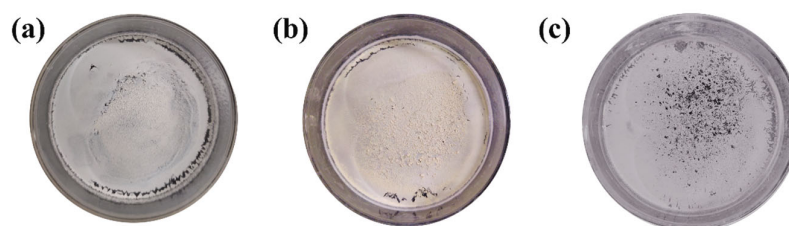

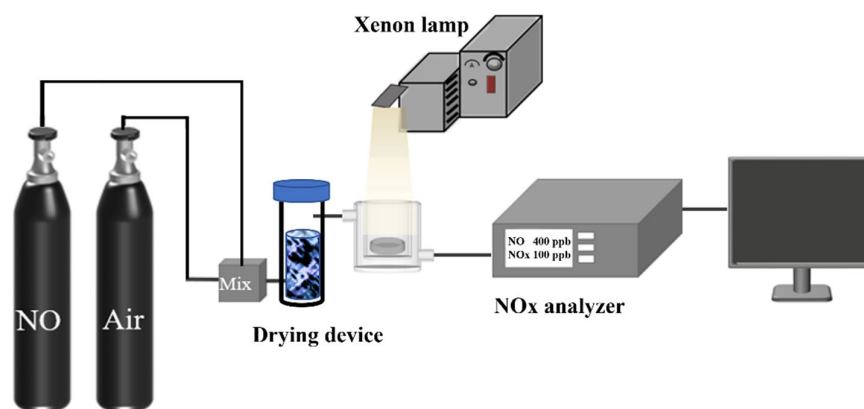**Figure 1.** Optical images of BNO (**a**), 2-BNO (**b**) and 2% Bi-2-BNO (**c**).

Figure 2. Experimental setup for the real-time monitoring and testing of photocatalytic NO removal.

2.5. Trapping Test

PBQ, TBA, K$_2$Cr$_2$O$_7$ and KI were used as effective scavengers to trap •O$_2$$^-$, •OH, e$^-$ and h$^+$, respectively [26]. Using an ultrasonic mixer, samples (50 mg) and 1 mmol of the trapping agents were uniformly mixed in 10 mL of deionized water. A homogenous film was then created by treating these combined suspensions at 60 °C in an oven.

3. Results and Discussion

3.1. Photocatalytic Efficiency

Under visible-light illumination ($\lambda > 420$ nm), the photocatalytic activity of the as-prepared samples was investigated for NO removal. The findings are shown in Figure 3. The best photocatalyst was determined based on the composition of the samples, and their catalytic activities under the default operational conditions. The NO content was kept constant following the dark adsorption equilibrium. The photocatalytic efficiency curves for the samples with different urea content are exhibited in Figure 3a. After 14 min of irradiation, BNO showed poor photocatalytic activity, with a 17.0% of NO removal efficiency. The surface of BNO was smooth and lacked pore defects, which led to a limited of NO adsorption. After 11 min of illumination, the NO adsorption efficiency gradually decreased owing to the fact that the adsorption active sites were occupied by the photocatalytic reaction product NO_3^-. When urea was added, Bi_3NbO_7 photoactivity improved in the following order: 2-BNO (37.5%) > 3-BNO (27.7%) > 1-BNO (32.5%). According to the obtained results, the urea content drastically influenced the Bi_3NbO_7 photocatalytic activity towards NO removal, and the best performance was recorded with 1.6 g of urea. We speculate that the porosity of Bi_3NbO_7 structures was improved in the presence of urea, which could improve the absorption capacity of NO, ameliorating the photocatalytic performance. The photocatalytic activity of the samples with different Bi contents were also tested under the same operational conditions, and the results are presented in Figure 3b. The NO removal efficiency for these samples followed the sequence: 2% Bi-2-BNO (60.3%) > 1% Bi-2-BNO (56.5%) > 4% Bi-2-BNO (43.3%) > 2-BNO (37.5%). It is worth noting that the C/C_0 ratio of 4% Bi-2-BNO increased after 9 min of irradiation, which was due to the fact that the generated NO_3^- ions accumulated around the Bi nanoparticles, resulting in the decrease of the catalytic active sites on the surface and a reduction of NO removal efficiency. The results showed that increasing the Bi content from 0 to 2% improved the NO removal efficiency. However, as the concentration increased to above 2%, the photocatalytic efficiency began to decline, with a 17% decrease for the sample with 4% Bi. This could be due to the improvement of the light-harvesting properties via the SPR effect exerted by an appropriate amount of Bi, whereas excessive Bi nanodots hindered the photocatalytic activity via decreasing the contact area between Bi_3NbO_7 active sites and incident photons during the photocatalytic process.
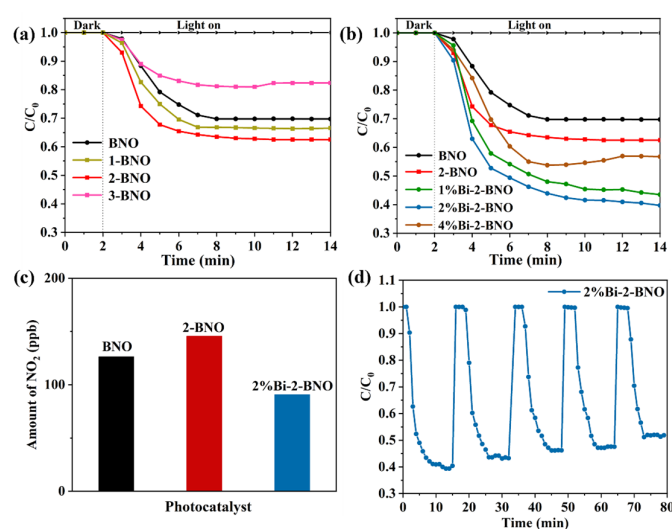

Figure 3. Photocatalytic activity of Bi_3NbO_7 with different contents of urea (**a**) and with different contents of Bi (**b**); NO_2 generation over the BNO, 2-BNO and 2% Bi-2-BNO samples under visible light (**c**); results of the recycling experiments with the 2% Bi-2-BNO photocatalyst (**d**).

Toxic by-products such as NO_2 are prone to be produced during the photocatalytic NO conversion process, which should be avoided as far as possible. In Figure 3c, NO_2 concentration for the BNO, 2-BNO and 2% Bi-2-BNO samples was 126, 146, and 91 ppb, respectively, which implied that the 2% Bi-2-BNO sample showed the best performance for converting NO and inhibiting NO_2 generation. The porous structure promoted the photocatalytic NO removal while increasing NO_2 production. However, the introduction of Bi nanodots in the pore-defective Ba_3NbO_7 significantly inhibited NO_2 production, indicating that metallic Bi was beneficial to enhance the photocatalytic oxidation capacity of the aforementioned photocatalyst, resulting in the complete conversion of NO. In real-world NOx removal, photocatalyst stability is of major concern. From the recycling experiments with the 2% Bi-2-BNO photocatalyst, it was seen that the photocatalytic yield decreased slightly (12% of reduction) after five run cycles (Figure 3d). This can be attributed to the formation of NO_3^- on the surface, which damaged the catalytic active sites. As shown in the SEM images before and after the stability test (Figure S1), there was no significant difference in the phase and morphology of 2% Bi-2-BNO, indicating that its stability was satisfactory.

3.2. Structural and Surface Characterizations

The XRD patterns of the prepared BNO, 1-BNO, 2-BNO and 3-BNO are shown in Figure 4a. The diffraction peaks of all samples could be well indexed as Bi_3NbO_7 crystalline phases (JCPDS PDF No.50-50078). Five typical diffraction peaks at 2θ = 28.16, 32.74, 46.73, 55.60 and 58.27°, were assigned to the (1 1 1), (200), (220), (311) and (222) planes, respectively. It is evident that pristine Bi_3NbO_7 was successfully synthesized in the presence of urea, and no other impurity peak appeared. As shown in Figure 4b, Bi displayed unique peaks at 2θ of 27.16, 37.95 and 39.62°, attributed to the planes (102), (104) and (110), respectively, according to the JCPDS Card No. 44-1246 [14]. The diffraction peaks of 1% Bi-2-BNO, 2% Bi-2-BNO and 4% Bi-2-BNO could be indexed as Bi and Bi_3NbO_7, indicating that Bi nanodots were successfully introduced in the pore-defective Bi_3NbO_7.
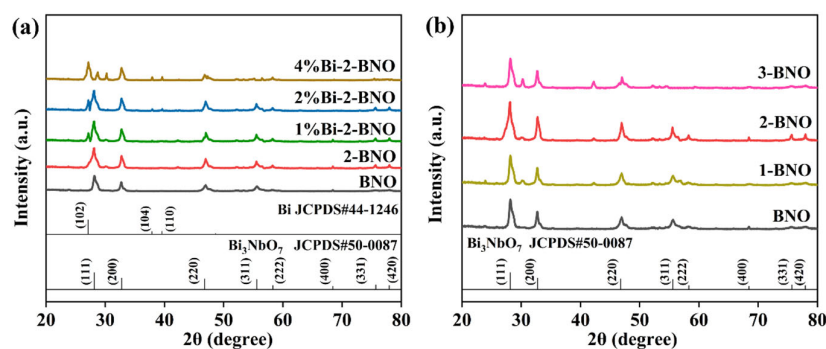

Figure 4. XRD patterns of the BNO photocatalyst with different amounts of urea (**a**) and of the 2-BNO sample with different amounts of Bi (**b**).

The optical properties of the samples were compared as shown in Figure 5a. The Bi nanoparticles-containing sample exhibited the highest optical absorption compared with the others. It was seen that the absorption edge of the 2-BNO sample showed a slight red shift compared with that of BNO, implying that the promotion of light absorption by the porous defects was small. In comparison with 2-BNO, an obvious increase of light absorption was achieved by the 2% Bi-2-BNO sample in the range of 300~800 nm, indicating that the presence of Bi nanoparticles was beneficial to the light absorption capacity of the pore-defective Bi_3NbO_7. Moreover, the formula $\alpha h\nu = A(h\nu - E_g)^{\eta/2}$ was used to estimate the band gap energy, where α is the absorption coefficient close to the absorption edge, h is the Planck constant, A is a constant, and Eg is the band gap energy (Figure 5b) [27]. The band gaps of BNO, 2-BNO and 2% Bi-2-BNO were calculated and shown to be 2.46, 2.42 and 2.05 eV, respectively. This decreasing band gap tendency for the samples was caused

by alterations in the electrical structure due to the combination of the pore defects and the SPR effect of Bi, which could facilitate visible light photoactivity.
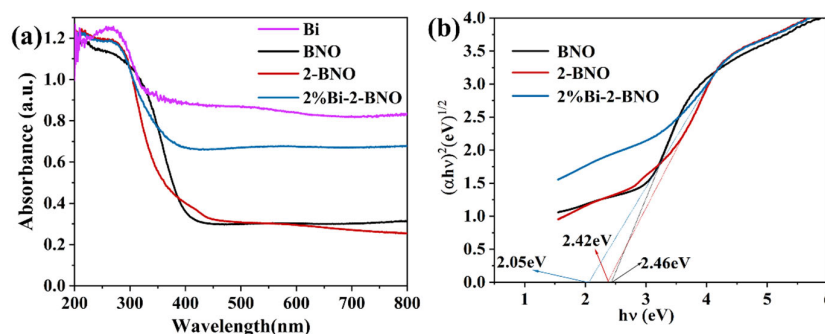

Figure 5. (**a**) Optical absorption spectra of the BNO, 2-BNO and 2% Bi-2-BNO samples and (**b**) the corresponding plots of $(\alpha h\upsilon)^{1/2}$ vs. energy (hυ).

SEM images served to examine the morphology and microstructure of the photocatalysts. As illustrated in Figure 6a,b, the BNO sample exhibited a smooth nanosheet morphology, and the average diameter and thickness of the nanoflowers were about 1μm and 50 nm, respectively. The 2-BNO sample exhibited a dense cluster morphology, and the diameter and thickness were similar to those of BNO (Figure 6c,d). The surface of the 2-BNO sample appeared rough and showed a porous structure, with pores having an average diameter of 50 nm, indicating that 2-BNO had successfully acquired porous defects after adding urea. The SEM images of 2% Bi-2-BNO are indicated in Figure 6e,f, which shows that the diameter and thicknesses were also similar to those of BNO and 2-BNO, but the 2% Bi-2-BNO morphology seemed looser than that of 2-BNO. As shown in the SEM images of 4% Bi-2-BNO (Figure S2), the structure of this sample was more compact, with more a clustered texture appearing on the surface, filling the porous defects. These observations imply that excess Bi would occupy the porous structure channels leading to a decrease in porous defects. As shown in Figure S3, the elemental mapping images indicated that Bi, Nb and O were uniformly distributed throughout the 2% Bi-2-BNO nanosheets. The weight percentages of the Bi, Nb and O elements were 75.36, 11.12, and 13.46%, respectively. More detailed information on the porous structure of the 2% Bi-2-BNO nanosheets could be deduced from the TEM images, Figure 6g, in which the Bi nanoparticles can be observed with the lattice space of 0.3210 nm and 0.3710 nm, corresponding to the (012) and (101) planes [28]. Additionally, the lattice fringes with a spacing of 0.2780 nm were attributed to the (200) facet of the Bi_3NbO_7 nanosheets [28]. Figure 6h depicts four crystalline planes, (111), (220), (200) and (400), for the BNO sample. It demonstrates that the synthesized BNO was in nanoscale. As displayed in Figure 6i, 2% Bi-2-BNO showed the (101) crystalline plane of Bi near the (200) plane of BNO, which corresponded to the TEM image, while this concentric circle was smaller than the concentric rings of BNO diffraction spot, indicating that the Bi nanoparticles were partly available in smaller sizes [28].

The nitrogen adsorption–desorption isotherms of the samples were type IV with typical hysteresis loops, as shown in Figure 7a. The hysteresis loops were of the H3 type at the relative pressure of 0.5~1.0 P/P_0, which is characteristic of nanosheet materials. Among all samples, 2% Bi-2-BNO had the highest specific surface area (S_{BET}), 47.22 m^2 g^{-1}, which facilitated NO adsorption on its surface. The S_{BET} values of the BNO and 2-BNO composites were found to be 18.24, and 27.45 m^2 g^{-1}, respectively. After the addition of urea and the insertion of Bi nanodots, the S_{BET} increased significantly, which was caused by increased surface roughness and the appearance of porous defects and a loose structure. As can be seen from the pore size distribution curves in Figure 7b, these samples contained mesopores (2–50 nm) and macropores (>50 nm). We inferred that the 2-BNO photocatalyst had higher photocatalytic activity than the nonporous BNO nanosheets due to its significantly porous structure. Moreover, the photocatalytic activity of 2% Bi-2-BNO

was higher than that of 2-BNO, resulting from the more active sites provided by the SPR effect due to the Bi nanoparticles.
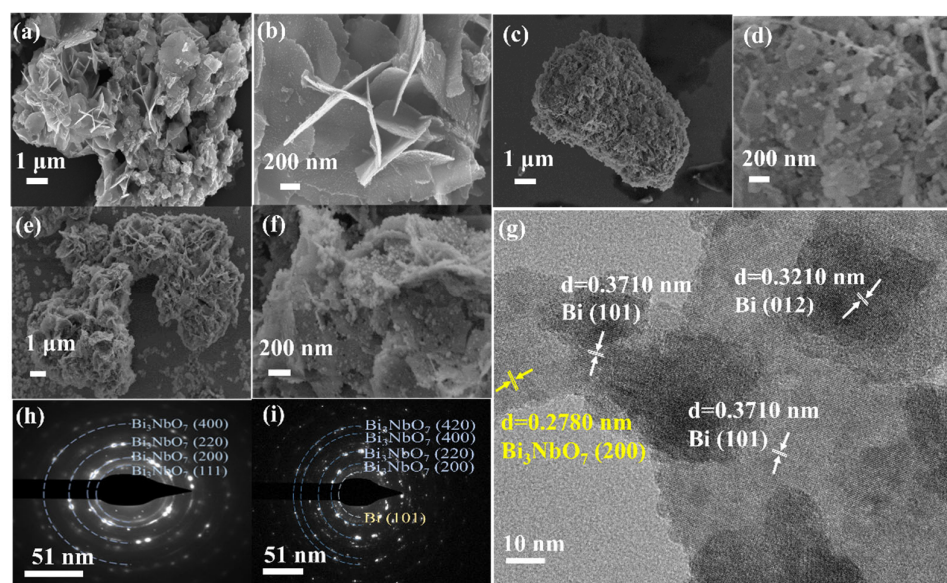

Figure 6. SEM images of (**a**,**b**) BNO, (**c**,**d**) 2-BNO and (**e**,**f**) 2% Bi-2-BNO; TEM images of 2% Bi-2-BNO nanosheets (**g**); SAED images of BNO (**h**) and 2% Bi-2-BNO (**i**).
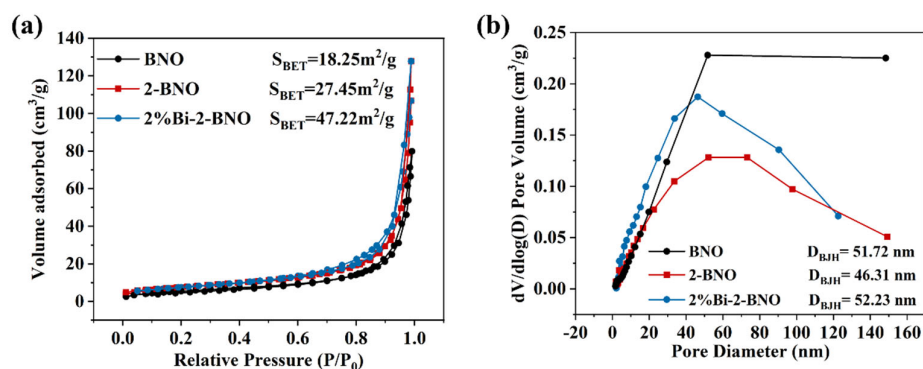

Figure 7. (**a**) N_2 adsorption–desorption isotherms for the photocatalytic samples, as well as (**b**) their pore size distribution curves.

Using X-ray photoelectron spectroscopy (XPS), the chemical state and composition of the BNO and 2% Bi-2-BNO photocatalysts were investigated. As shown in Figure 8a, the survey spectra revealed that the aforementioned samples contained Bi, Nb and O elements. As seen in the high-resolution Bi 4f spectra of BNO, the peaks of Bi $4f_{7/2}$ and $4f_{5/2}$ were positioned at about 158.7 and 164.01 eV and attributed to the Bi^{3+} chemical state [29]. In the Bi 4f spectra of 2% Bi-2-BNO (Figure 8b), two characteristic peaks were located at 158.97 and 164.34 eV, corresponding to Bi^{3+} $4f_{7/2}$ and $4f_{5/2}$ [30]. Metallic Bi was observed at 158.00 and 163.57 eV, demonstrating the existence of zero-valent Bi in 2% Bi-2-BNO [31]. The Nb 3d XPS spectrum for BNO displayed two peaks located at binding energy values of 206.43 and 209.18 eV, which were assigned to Nb $3d_{3/2}$ and $3d_{5/2}$, respectively [32]. In Figure 8c, the peaks positioned at about 206.57 and 209.34 eV correspond to Nb^{5+} [33]. The high-resolution scan of the O 1s spectrum of BNO showed some peaks located at about 529.30 and 531.03 eV, which were attributed to the Bi-O and Nb-O bonds, respectively [14]. Compared with BNO, three peaks could be observed in the O 1s XPS spectra of 2% Bi-2-BNO (Figure 8d), with an additional peak at the lattice oxygen's binding energy of 531.03 eV [34]. The binding energies of Bi, Nb and O were shifted to the high binding

energy side after the growth of metallic Bi, which might be the result of a partial electron transfer to it [27].
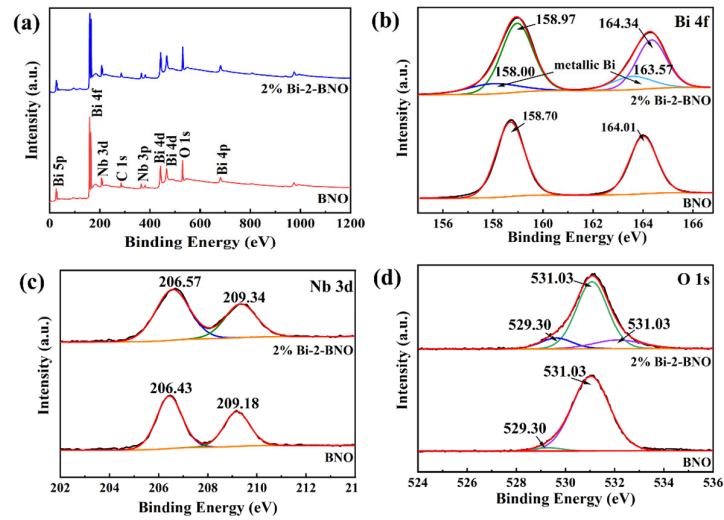

Figure 8. XPS analysis of the BNO and 2% Bi-2-BNO samples: (**a**) survey spectra, (**b**) Bi 4f, (**c**) Nb 3d and (**d**) O 1s.

The transient photocurrent responses for electrodes coated with BNO, 2-BNO and 2% Bi-2-BNO under visible light irradiation were investigated to better understand the behavior of photoinduced charges (Figure 9a). The corresponding pattern for 2-BNO appeared obviously at higher responses compared with that of BNO, indicating that the porous defects could improve the separation efficiency of the photogenerated electron-hole pairs. Furthermore, the photocurrent response of the 2% Bi-2-BNO sample was much higher than those of the others, as expected. The results suggest that the Bi SPR effect accelerated the migration of the charge carriers at the zero-dimensional/two-dimensional interfaces, which was highly favorable to charge separation, resulting in a better photocatalytic performance. The EIS Nyquist plots are shown in Figure 9b. The arc radius of BNO, 2-BNO and 2% Bi-2-BNO decreased sequentially, implying that the charge transfer resistance also decreased in a similar manner.
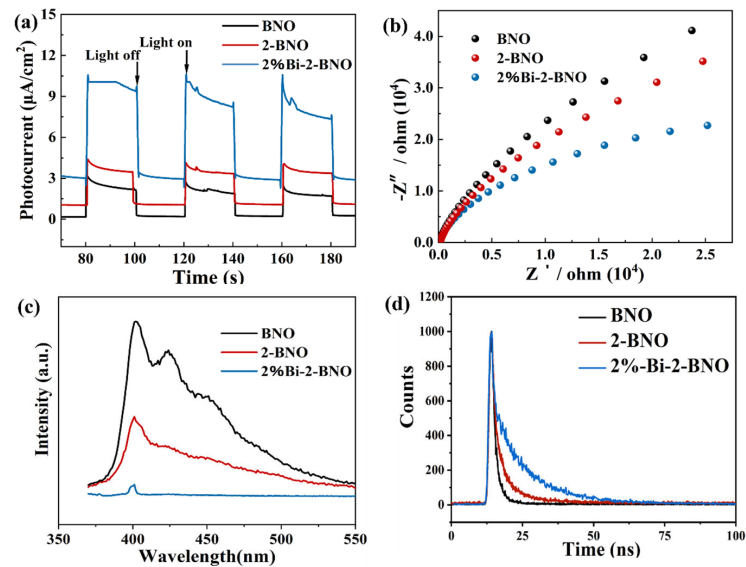

Figure 9. (**a**) Transient photocurrent responses; (**b**) EIS spectra of the as-prepared samples; (**c**) photoluminescence spectra; (**d**) time-resolved photoluminescence spectra of the photocatalysts.

Fluorescence spectroscopy and time-resolved transient fluorescence spectroscopy were used to explore the separation efficiency of the photogenerated charge carriers. A weaker PL intensity frequently indicates a lower charge carriers' recombination rate. The pristine BNO and the 2% Bi-2-BNO samples exhibited the strongest and the weakest PL emission intensity, respectively (Figure 9c). This quenching effect could be owed to the presence of more active sites because of the porous defects and metallic Bi, which raised the chance of charge separation and suppressed their recombination, thus improving the photocatalytic activity. As presented in Figure 9d, the average fluorescence lifetimes (τ_{ave}) of BNO, 2-BNO and 2% Bi-2-BNO were estimated to be 2.3, 5.02 and 5.28 ns, respectively. The prolonged τ_{ave} value of 2% Bi-2-BNO suggests that the porous flaws and metallic Bi promoted the effective separation of the photogenerated charge carriers.

3.3. Photocatalytic Mechanism

Electron paramagnetic resonance (EPR) measurements were carried out to detect the reactive oxygen species during photocatalysis. As shown in Figure 10a,b, no EPR signal was observed in the dark, but the superoxide radical ($\bullet O_2^-$) and the hydroxyl radical ($\bullet OH$) signals appeared after 5 min of light irradiation for the 2% Bi-2-BNO sample [35,36], indicating that both reactive oxygen species played a key role throughout the photocatalytic elimination of NO over the aforementioned photocatalyst. To further justify the results of the EPR analysis and the effectiveness of the mentioned primary active ingredients during the photocatalytic pathway, trapping tests were conducted for 2% Bi-2-BNO. PBQ, TBA, $K_2Cr_2O_7$ and KI were chosen to trap $\bullet O_2^-$, $\bullet OH$, e^- and h^+, respectively. According to Figure 10c, the addition of PBQ, $K_2Cr_2O_7$ and KI clearly retarded the NO conversion, demonstrating that the photocatalytic conversion mechanism depended predominantly on $\bullet O_2^-$, e^- and h^+. However, when TBA was used, the NO removal efficiency did not obviously decrease, suggesting that $\bullet OH$ rarely participated in the photocatalytic NO removal process.
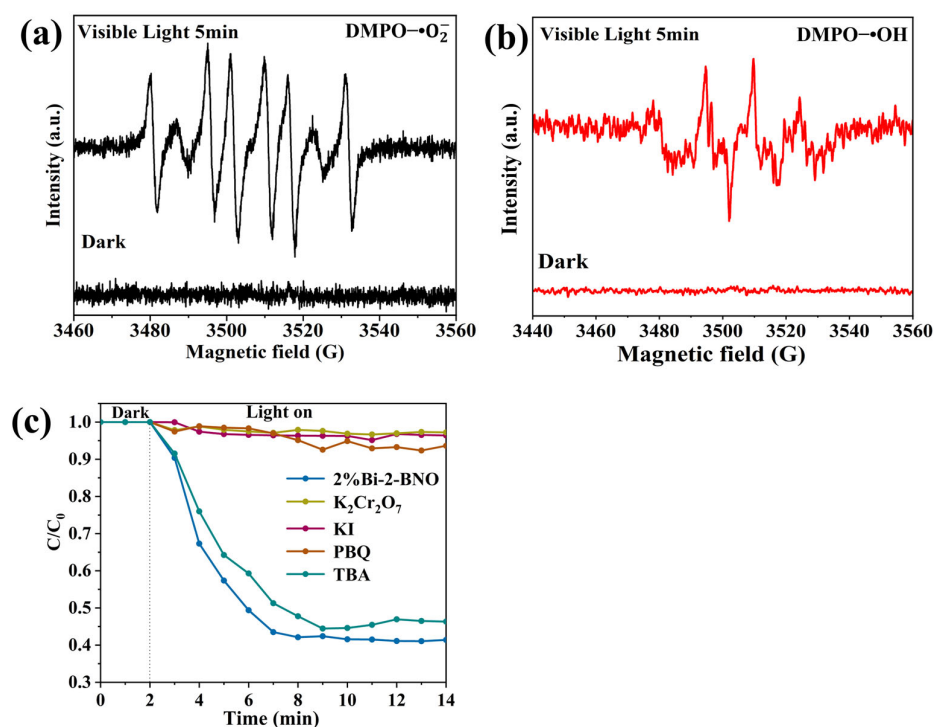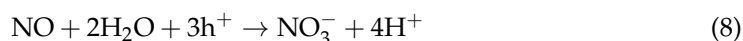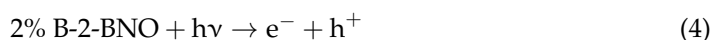

Figure 10. EPR spectra of the (**a**) DMPO−$\bullet O_2^-$ and (**b**) DMPO−$\bullet OH$ adducts under dark and irradiation; (**c**) effect of different radical scavengers on NO removal using 2% Bi-2-BNO.

According to the abovementioned findings, a plausible mechanism for the photocatalytic NO removal using 2% Bi-2-BNO is as follow:

$$2\% \text{ B-2-BNO} + h\nu \rightarrow e^- + h^+ \tag{4}$$

$$O_2 + e^- \rightarrow \bullet O_2^- \tag{5}$$

$$NO + \bullet O_2^- \rightarrow NO_3^- \tag{6}$$

$$2NO + O_2 \rightarrow 2NO_2 \tag{7}$$

$$NO + 2H_2O + 3h^+ \rightarrow NO_3^- + 4H^+ \tag{8}$$

$$O_2^- + 2H_2O + e^- \rightarrow H_2O_2 + 2OH^- \tag{9}$$

$$H_2O_2 + e^- \rightarrow \bullet OH + OH^- \tag{10}$$

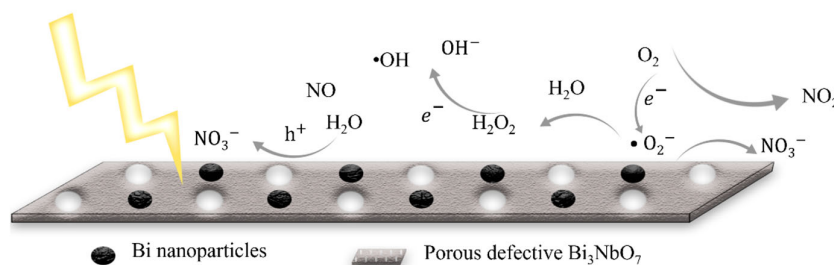This pathway is schematically illustrated in Figure 11.

Figure 11. Reaction mechanism diagram of the photocatalytic NO removal by the 2% Bi-2-BNO photocatalyst.

4. Conclusions

Concisely, photocatalytic pore-defective Bi/Bi$_3$NbO$_7$ nanosheets were successfully synthesized via the solvothermal method. Using urea during the synthesis steps, the Bi$_3$NbO$_7$ microstructure and porosity were serendipitously affected, leading to a 20.5% improvement of the photocatalytic efficiency towards NO removal. Furthermore, it was demonstrated that the growth of Bi nanodots along with the increase in porosity enhanced the photocatalytic activity of the materials. The highest NO removal efficiency, 60.3%, was obtained over the pore-defective Bi@Bi$_3$NbO$_7$ when the molar ratios of urea and Bi(NO)$_3 \bullet 5$H$_2$O to pristine Bi$_3$NbO$_7$ were 1:25 and 1:2, respectively, and was two times higher than that of BNO in the same conditions. In brief, the combination of porous defects and the SPR effect of the Bi nanoparticles ameliorated the visible light-harvesting properties, delayed the electron-hole recombination, and provided more efficient active sites on the surface, resulting in a better photocatalytic performance, while the generation of the toxic by-product NO$_2$ was significantly inhibited. More importantly, NO was predominantly converted to NO$_3^-$, and $\bullet$O$_2^-$, e$^-$ and h$^+$ played a key role in the prepared photocatalysts, with a minor contribution of $\bullet$OH radicals. The present work provides new insights for the removal of NO, especially for minimizing the generation of toxic byproducts during this process.

Author Contributions: Conceptualization, T.G. and J.L.; Investigation, T.G., J.L. and W.Z.; Methodology, J.L., K.Z. and M.S.; Project administration, C.W.; Visualization, T.G., J.L. and Y.Z.; Writing—original draft, T.G., J.L., M.P. and C.W.; Writing—review and editing, T.G., J.L. and C.W. All authors have read and agreed to the published version of the manuscript.

Institutional Review Board Statement: No ethical approval was required for the present work.

Data Availability Statement: Not applicable.

Conflicts of Interest: On behalf of all authors, the corresponding author states that there is no conflict of interest.

References

1. Li, N.; Shi, M.; Xin, Y.; Zhang, W.; Qin, J.; Zhang, K.; Lv, H.; Yuan, M.; Wang, C. Oxygen vacancies-modified S-scheme $Bi_2Ti_2O_7$/$CaTiO_3$ heterojunction for highly efficient photocatalytic NO removal under visible light. *J. Environ. Chem. Eng.* **2022**, *10*, 107420. [CrossRef]
2. Li, X.; Dong, G.; Guo, F.; Zhu, P.; Huang, Y.; Wang, C. Enhancement of photocatalytic NO removal activity of g-C_3N_4 by modification with illite particles. *Environ. Sci.-Nano* **2020**, *7*, 1990–1998. [CrossRef]
3. Li, N.; Wang, C.; Zhang, K.; Lv, H.; Yuan, M.; Bahnemann, D.W. Progress and prospects of photocatalytic conversion of low-concentration NOx. *Chin. J. Catal.* **2022**, *43*, 2363–2387. [CrossRef]
4. Zhu, Q.; Hailili, R.; Xin, Y.; Zhou, Y.; Huang, Y.; Pang, X.; Zhang, K.; Robertson, P.K.J.; Bahnemann, D.W.; Wang, C. Efficient full spectrum responsive photocatalytic NO conversion at $Bi_2Ti_2O_7$: Co-effect of plasmonic Bi and oxygen vacancies. *Appl. Catal. B Environ.* **2022**, *319*, 121888. [CrossRef]
5. Yang, W.; Ren, Q.; Zhong, F.; Wang, Y.; Wang, J.; Chen, R.; Li, J.; Dong, F. Promotion mechanism of -OH group intercalation for NOx purification on BiOI photocatalyst. *Nanoscale* **2021**, *13*, 20601–20608. [CrossRef] [PubMed]
6. Gao, T.; Zhang, K.; Zhu, Q.; Tian, Q.; Wang, H.; Zhang, W.; Liang, J.; Lin, J.; Allam, A.A.; Ajarem, J.S.; et al. One Step Synthesis of Oxygen Defective Bi@Ba_2TiO_4/$BaBi_4Ti_4O_{15}$ Microsheet with Efficient Photocatalytic Activity for NO Removal. *Catalysts* **2022**, *12*, 1455. [CrossRef]
7. Duan, Y.; Luo, J.; Zhou, S.; Mao, X.; Shah, M.W.; Wang, F.; Chen, Z.; Wang, C. TiO_2-supported Ag nanoclusters with enhanced visible light activity for the photocatalytic removal of NO. *Appl. Catal. B Environ.* **2018**, *234*, 206–212. [CrossRef]
8. Wang, C.-y.; Böttcher, C.; Bahnemann, D.W.; Dohrmann, J.K. In situ Electron Microscopy Investigation of Fe(III)-doped TiO_2 Nanoparticles in an Aqueous Environment. *J. Nanoparticle Res.* **2004**, *6*, 119–122. [CrossRef]
9. Li, Y.; Dang, L.; Han, L.; Li, P.; Wang, J.; Li, Z. Iodine-sensitized $Bi_4Ti_3O_{12}$/TiO_2 photocatalyst with enhanced photocatalytic activity on degradation of phenol. *J. Mol. Catal. A Chem.* **2013**, *379*, 146–151. [CrossRef]
10. Hao, L.; Yan, J.; Guan, S.; Cheng, L.; Zhao, Q.; Zhu, Z.; Wang, Y.; Lu, Y.; Liu, J. Oxygen vacancies in TiO_2/SnO_x coatings prepared by ball milling followed by calcination and their influence on the photocatalytic activity. *Appl. Surf. Sci.* **2019**, *466*, 490–497. [CrossRef]
11. Duan, Y.; Zhang, M.; Wang, L.; Wang, F.; Yang, L.; Li, X.; Wang, C. Plasmonic Ag-TiO_{2-x} nanocomposites for the photocatalytic removal of NO under visible light with high selectivity: The role of oxygen vacancies. *Appl. Catal. B Environ.* **2017**, *204*, 67–77. [CrossRef]
12. Lu, Y.; Chen, M.; Huang, T.; Huang, Y.; Cao, J.-j.; Li, H.; Ho, W.; Lee, S.C. Oxygen vacancy-dependent photocatalytic activity of well-defined $Bi_2Sn_2O_{7-x}$ hollow nanocubes for NOx removal. *Environ. Sci.-Nano* **2021**, *8*, 1927–1933. [CrossRef]
13. Wang, Q.; Yuan, L.; Dun, M.; Yang, X.; Chen, H.; Li, J.; Hu, J. Synthesis and characterization of visible light responsive Bi_3NbO_7 porous nanosheets photocatalyst. *Appl. Catal. B Environ.* **2016**, *196*, 127–134. [CrossRef]
14. Wang, K.; Li, Y.; Zhang, G.; Li, J.; Wu, X. 0D Bi nanodots/2D Bi_3NbO_7 nanosheets heterojunctions for efficient visible light photocatalytic degradation of antibiotics: Enhanced molecular oxygen activation and mechanism insight. *Appl. Catal. B Environ.* **2019**, *240*, 39–49. [CrossRef]
15. Zhang, S.; Yang, Y.; Guo, Y.; Guo, W.; Wang, M.; Guo, Y.; Huo, M. Preparation and enhanced visible-light photocatalytic activity of graphitic carbon nitride/bismuth niobate heterojunctions. *J. Hazard. Mater.* **2013**, *261*, 235–245. [CrossRef]
16. Liu, G.; Huang, Y.; Lv, H.; Wang, H.; Zeng, Y.; Yuan, M.; Meng, Q.; Wang, C. Confining single-atom Pd on g-C_3N_4 with carbon vacancies towards enhanced photocatalytic NO conversion. *Appl. Catal. B Environ.* **2021**, *284*, 119683. [CrossRef]
17. Liu, J.; Bunes, B.R.; Zang, L.; Wang, C. Supported single-atom catalysts: Synthesis, characterization, properties, and applications. *Environ. Chem. Lett.* **2018**, *16*, 477–505. [CrossRef]
18. Li, Y.; Wen, M.; Wang, Y.; Tian, G.; Wang, C.; Zhao, J. Plasmonic Hot Electrons from Oxygen Vacancies for Infrared Light-Driven Catalytic CO_2 Reduction on Bi_2O_{3-x}. *Angew. Chem. Int. Ed.* **2021**, *60*, 910–916. [CrossRef]

19. Rej, S.; Santiago, E.Y.; Baturina, O.; Zhang, Y.; Burger, S.; Kment, S.; Govorov, A.O.; Naldoni, A. Colloidal titanium nitride nanobars for broadband inexpensive plasmonics and photochemistry from visible to mid-IR wavelengths. *Nano Energy* **2022**, *104*, 107989. [CrossRef]

20. Bayles, A.; Tian, S.; Zhou, J.; Yuan, L.; Yuan, Y.; Jacobson, C.R.; Farr, C.; Zhang, M.; Swearer, D.F.; Solti, D.; et al. Al@TiO$_2$ Core–Shell Nanoparticles for Plasmonic Photocatalysis. *ACS Nano* **2022**, *16*, 5839–5850. [CrossRef]

21. Xiao, K.; Liu, H.; Li, Y.; Yang, G.; Wang, Y.; Yao, H. Excellent performance of porous carbon from urea-assisted hydrochar of orange peel for toluene and iodine adsorption. *Chem. Eng. J.* **2020**, *382*, 122997. [CrossRef]

22. Xu, Y.; Li, H.; Sun, B.; Qiao, P.; Ren, L.; Tian, G.; Jiang, B.; Pan, K.; Zhou, W. Surface oxygen vacancy defect-promoted electron-hole separation for porous defective ZnO hexagonal plates and enhanced solar-driven photocatalytic performance. *Chem. Eng. J.* **2020**, *379*, 122295. [CrossRef]

23. Song, P.; Sun, S.; Cui, J.; Zheng, X.; Liang, S. Organic dye-reformed construction of porous-defect g-C$_3$N$_4$ nanosheet for improved visible-light-driven photocatalytic activity. *Appl. Surf. Sci.* **2021**, *568*, 150986. [CrossRef]

24. Zhou, Y.; Ren, X.; Du, Y.; Jiang, Y.; Wan, J.; Ma, F. In-situ template cooperated with urea to construct pectin-derived hierarchical porous carbon with optimized pore structure for supercapacitor. *Electrochim. Acta* **2020**, *355*, 136801. [CrossRef]

25. Wang, S.; Dong, L.; Li, Z.; Lin, N.; Xu, H.; Gao, S. Sustainable supercapacitors of nitrogen-doping porous carbon based on cellulose nanocrystals and urea. *Int. J. Biol. Macromol.* **2020**, *164*, 4095–4103. [CrossRef] [PubMed]

26. Shi, M.; Rhimi, B.; Zhang, K.; Xu, J.; Bahnemann, D.W.; Wang, C. Visible light-driven novel Bi$_2$Ti$_2$O$_7$/CaTiO$_3$ composite photocatalyst with enhanced photocatalytic activity towards NO removal. *Chemosphere* **2021**, *275*, 130083. [CrossRef]

27. Zhang, W.; Zhao, J.; Allam, A.A.; Xin, Y.; Lin, J.; Gao, T.; Ajarem, J.S.; Li, X.; Wang, C.; Bahnemann, D.W. Palladium Nanoparticles Embedded Nutshell-like Bi$_2$WO$_6$ as an Efficient and Stable Visible-Light-Responsive Photocatalysts for NO Removal. *Energy Fuels* **2022**, *36*, 13852–13862. [CrossRef]

28. Gan, H.; Zhang, G.; Huang, H. Enhanced visible-light-driven photocatalytic inactivation of Escherichia coli by Bi$_2$O$_2$CO$_3$/Bi$_3$NbO$_7$ composites. *J. Hazard. Mater.* **2013**, *250–251*, 131–137. [CrossRef]

29. Saeed, N.A.M.; Coetsee, E.; Kroon, R.E.; Bettinelli, M.; Swart, H.C. Photoluminescence of Bi^{3+} doped in YOF phosphor as an activator. *Opt. Mater.* **2021**, *119*, 111291. [CrossRef]

30. Chu, H.; Zhang, Z.; Song, Z.; Du, A.; Dong, S.; Li, G.; Cui, G. Facilitated magnesium atom adsorption and surface diffusion kinetics via artificial bismuth-based interphases. *Chem. Commun.* **2021**, *57*, 9430–9433. [CrossRef]

31. Eraky, M.S.; Sanad, M.M.S.; El-Sayed, E.M.; Shenouda, A.Y.; El-Shereafy, E.-S. Influence of the electrochemical processing parameters on the photocurrent–voltage conversion characteristics of copper bismuth selenide photoactive films. *Eur. Phys. J. Plus* **2022**, *137*, 907. [CrossRef]

32. Jiang, D.; Sun, X.; Wu, X.; Zhang, S.; Qu, X.; Shi, L.; Zhang, Y.; Du, F. MXene-Ti$_3$C$_2$ assisted one-step synthesis of carbon-supported TiO$_2$/Bi$_4$NbO$_8$Cl heterostructures for enhanced photocatalytic water decontamination. *Nanophotonics* **2020**, *9*, 2077–2088. [CrossRef]

33. Batoo, K.M.; Verma, R.; Chauhan, A.; Kumar, R.; Hadi, M.; Aldossary, O.M.; Al-Douri, Y. Improved room temperature dielectric properties of Gd^{3+} and Nb^{5+} co-doped Barium Titanate ceramics. *J. Alloys Compd.* **2021**, *883*, 160836. [CrossRef]

34. Zhang, X.; Yu, S.; Liu, Y.; Zhang, Q.; Zhou, Y. Photoreduction of non-noble metal Bi on the surface of Bi$_2$WO$_6$ for enhanced visible light photocatalysis. *Appl. Surf. Sci.* **2017**, *396*, 652–658. [CrossRef]

35. Sun, J.; Wang, L.; Wang, Y.; Lv, W.; Yao, Y. Activation of peroxymonosulfate by MgCoAl layered double hydroxide: Potential enhancement effects of catalyst morphology and coexisting anions. *Chemosphere* **2022**, *286*, 131640. [CrossRef]

36. Zhu, Q.; Dar, A.A.; Zhou, Y.; Zhang, K.; Qin, J.; Pan, B.; Lin, J.; Patrocinio, A.O.T.; Wang, C. Oxygen Vacancies Promoted Piezoelectricity toward Piezo-Photocatalytic Decomposition of Tetracycline over SrBi$_4$Ti$_4$O$_{15}$. *ACS EST Eng.* **2022**, *2*, 1365–1375. [CrossRef]